mater.scichina.com link.springer.com

Published online 8 June 2022 | https://doi.org/10.1007/s40843-021-2047-x
Sci China Mater 2022, 65(9): 2363–2372

Nitrogen and phosphorous co-doped hierarchical meso–microporous carbon nanospheres with extraordinary lithium storage for high-performance lithium-ion capacitors

Tong Li[1†], Jianjun Zhang[1†], Chongxing Li[1], Han Zhao[1], Jing Zhang[2*], Zhao Qian[1*], Longwei Yin[1] and Rutao Wang[1,3,4*]

ABSTRACT **Lithium-ion capacitors (LICs), consisting of a battery-like negative electrode and a capacitive porous-carbon positive electrode, deliver more than twice the energy density of electric double-layer capacitors. However, their wide application suffers from low energy density and reduced cycle life at high rates. Herein, hierarchical meso–microporous carbon nanospheres with a highly disordered structure and nitrogen/phosphorous co-doped properties were synthesized through a facile template method. Such hierarchical porous structure facilitates rapid ion transport, and the highly disordered structure and high heteroatom content provide abundant active sites for Li^+ charge storage. Electrochemical experiments demonstrated that the carbon nanosphere anode delivers large reversible capability, greatly improves rate capability and exhibits excellent cycle stability. An LIC fabricated with the carbon nanosphere anode and an activated carbon cathode yields a high energy density of 103 W h kg^{-1}, an extremely high power density of 44,630 W kg^{-1}, and long-term cyclability of over 10,000 cycles. This work presents how structural control of carbon materials at the nano/atomic scale can significantly enhance electrochemical performance, enabling new opportunities for the design of high-performance energy-storage devices.**

Keywords: lithium-ion capacitors, porous carbon, anode, heteroatoms doping, energy storage devices

INTRODUCTION

Owing to their merits in delivering both high energy and power density as well as long cycle life, lithium-ion capacitors (LICs) have been considered a promising technology to meet the requirements of portable electronics, hybrid electric vehicles, and large-scale grid storage [1,2]. Electrode materials are the heart of LICs: Li^+ ions are reversibly inserted in/deserted out of a battery-like anode, whereas counter anions are adsorbed/desorbed on the surface of a capacitive activated carbon cathode. Compared with well-studied activated carbon cathodes, anode materials with a high specific capacity, good rate capability, and long-term cycle stability have been the focus of research. To date, various anode materials have been explored to promote the development of LICs, mainly including alloy-, redox-, and insert-type materials [3]. Alloy- and redox-type electrode materials possess high specific capacity, but they suffer from large volume change and poor cycle stability [4]. By contrast, insert-type anodes show no phase change during constant Li^+ intercalated-deintercalated processes, enabling LICs with long-term cycle stability [5]. Moreover, insert-type anodes with a size scale in the order of nanometers usually exhibit pseudocapacitive properties, where the kinetics is not diffusion-limited and thus fast [5–7]. So far, substantial progress in insert-type anode designs has been carried out to realize high-performance LICs.

Carbonaceous materials, as typical insert-type materials, are competitive candidates for LIC anode because of their advantages, including low cost, high conductivity, environmental friendliness, and low Li^+ intercalation potential [8–10]. The most common carbon anode is graphite for LICs. However, the relatively low capacity of 372 mA h g^{-1} and inferior kinetics of graphite are the major drawbacks and subsequently limit the energy and power output of LICs [11]. Several strategies have been proposed to solve these issues. One of these is the introduction of nanoscale pores into a carbon matrix to increase the surface area and shorten the Li^+ diffusion path, which is kinetically favorable for ion transport [12–14]. Another strategy is heteroatom doping at the atomic level, which is beneficial to improving Li^+ charge storage properties [15]. Research studies found that heteroatom dopants, such as O [16], N [17–20], P [21,22], S [23–25], and B [26], have multiple functions, including changing carbon structure, enhancing electronic conductivity, and introducing more defects and reactive sites for Li^+ [27]. In some cases, these effects worked synergically, e.g., heteroatom-rich carbon anodes would feature pseudocapacitive Li^+ storage properties, largely improving rate capability [28]. Inspired by these strategies, structural control of carbon mate-

[1] Key Laboratory for Liquid-Solid Structural Evolution and Processing of Materials, Ministry of Education, School of Materials Science and Engineering, Shandong University, Jinan 250061, China
[2] Shandong Key Laboratory for Special Silicon-containing Material, Advanced Materials Institute, Qilu University of Technology (Shandong Academy of Sciences), Jinan 250014, China
[3] Suzhou Institute of Shandong University, Suzhou 215123, China
[4] CAS Key Laboratory of Carbon Materials, Institute of Coal Chemistry, Chinese Academy of Sciences, Taiyuan 030001, China
[†] These authors contributed equally to this work.
[*] Corresponding authors (emails: rtwang@sdu.edu.cn (Wang R); zhangjing@sdas.org (Zhang J); qianzhao@sdu.edu.cn (Qian Z))

rials through constructing porous architectures and heteroatom doping at the nano/atomic scale is highly preferable to solve the kinetics and capacity limitations of carbon anodes and further improve the electrochemical performance of LICs.

Here, we report a template method for the facile fabrication of nitrogen and phosphorous co-doped hierarchical meso–microporous carbon nanospheres (N/P-HMCNs) simply by pyrolysis of a silica-polyaniline (PANi) core-shell composite obtained through template polymerization of aniline in the presence of phytic acid. The as-prepared N/P-HMCNs show exceptional Li^+ charge-storage properties over commercial graphite and hard carbon. As a result, LICs assembled with the N/P-HMCN anode yield high energy and power densities as well as long-term cycle stability.

EXPERIMENTAL SECTION

Material synthesis

Ludox AM-40 silica colloid solution (average size ~20 nm) was purchased from Sigma-Aldrich (St. Louis, MO, USA). Aniline (guaranteed reagent, >99.9%), phytic acid solution (analytical reagent (AR), 70%), ammonium persulfate (AR, >98%), hydrofluoric acid (AR, 40%), and hydrochloric acid (AR, 37%) were purchased from Shanghai Aladdin Bio-Chem Technology Co., Ltd. All chemicals were used as received without further purification.

Typically, silica colloid (2.5 g, 40 wt%), aniline (0.5 mL), and phytic acid (3.2 mL) were mixed in 100 mL of distilled water for about 1 h at 4°C. Then, ammonium persulfate (0.6 g) was dissolved in 10 mL of distilled water and was added to the above mixture solution with vigorous stirring for more than 12 h. Subsequently, a dark green suspension consisting of PANi spheres was formed. The PANi spheres were collected by centrifugation and then dried in a freezer dryer for 48 h. They were then placed in a vacuum tube furnace under argon atmosphere and heated to 1000°C at a heating rate of 5°C min^{-1} for 1 h to obtain a black carbonized powder. Subsequently, 5 mL of 40% hydrofluoric (HF) acid was mixed with the carbonized powder, and the mixture was stirred for 2 h to remove the SiO_2 template. Then, the carbon powder was collected by filtration with water to remove HF acid and then dried in an oven at 60°C for 8 h. The final porous carbon product was designated as N/P-HMCN. For comparison, nitrogen-doped ordered HMCNs (N-HMCNs) were prepared through the above procedure without the addition of phytic acid. For this procedure, aqueous HCl solution (1 mol L^{-1}) was used instead of phytic acid and was added dropwise to the previously prepared solution until the pH value of the solution reached 3.

Material characterization

Field emission scanning electron microscopy (FESEM, SU-70, Hitachi, Japan) and transmission electron microscopy (TEM, Tecnai F20, FEI Company, Hillsboro, OR, USA) were carried out to investigate the morphology and structure of the as-prepared samples. The structure and composition of the samples were studied by powder X-ray diffraction (XRD, D/Max 2400, Rigaku, Tokyo, Japan) using Cu-Kα radiation. A micro-Raman spectroscope (JY-HR800, excitation wavelength of 532 nm) was used to obtain the Raman spectra of the samples. X-ray photoelectron spectroscopy (XPS, PHI-5702 spectrometer, PerkinElmer, Waltham, MA, USA) was employed to record the surface chemical species of the samples. The pore structure data of the samples were obtained using an ASAP 2020 volumetric adsorption analyzer (Micromeritics, Norcross, GA, USA) at 77 K.

Electrode preparation

For the fabrication of a N/P-HMCN anode, 80 wt% N/P-HMCN active material, 10 wt% acetylene black (as the conducting filler), and 10 wt% polyvinylidene fluoride in *N*-methyl-2-pyrrolidone (as a binder) were mixed in a mortar. The well-mixed slurry was homogeneously coated on a copper foil with a mass loading of 0.8–1.0 mg. The copper foil coated with the slurry was dried at 110°C in a vacuum. For half cells, the N/P-HMCN anode was tested using a coin-type cell (2032 type), and a Li metal foil was used as the counter and reference electrodes. Before the fabrication of LIC hybrid cells (or full cells), the N/P-HMCN anode was charged-discharged for several cycles and ended in a lithiated state at 0.01 V under a current density of 0.1 A g^{-1} in a half cell, and then it was detached in an Ar-filled glovebox. The prelithiated N/P-HMCN anode coupled with a fabricated PANi-derived porous carbon (PDPC) cathode was assembled in a 2032-type coin cell, which was separated by a round glass fiber membrane (Whatman, Cytiva, Marlborough, MA, USA). For both half and full cells, 1 mol L^{-1} $LiPF_6$ in ethylene carbonate/dimethyl carbonate/ethyl methyl carbonate (EC/DMC/EMC = 1:1:1 vol%) with 2.0% fluoroethylene carbonate (FEC) was employed as the electrolyte. The average dosage of electrolytes for the half and full cells was about 80 μL. The half and full cells were assembled in an Ar-filled glovebox with low H_2O and O_2 levels (less than 0.1 ppm).

Electrochemical measurements

Cyclic voltammetry (CV) test, galvanostatic charge-discharge measurements, and electrical impedance spectroscopy (EIS) were recorded using a CHI760E instrument (CH Instruments, Inc., Shanghai, China). For the life-span tests for half and hybrid cells, a battery test system (Land CT2001A model, Wuhan Land Electronics, Ltd., Wuhan, China) was used.

The energy density (E, W h kg^{-1}) of LICs can be calculated using the constant discharge current (I), cell voltage (V), and start and end discharging time (t_1 and t_2) according to the following equation:

$$E = \int_{t_1}^{t_2} IV \, dt. \quad (1)$$

The power density (P, in W kg^{-1}) of LICs can be calculated using energy density (E) and discharging time (t) according to the following equation:

$$P = E / t. \quad (2)$$

Density functional theory computation details

Density functional theory (DFT) calculations were implemented wtih Vienna *Ab Initio* Simulation Package. The Perdew-Burke-Ernzerhof generalized gradient approximation was employed to describe the electron interaction as exchange correlation functional. Grimme's semiempirical DFT-D3 scheme was used in computations to produce a better description of long-range van der Waals interactions. The plane-wave basis set with an energy cutoff of 500 eV was applied in all calculations. The optimized structures were obtained using a conjugate gradient algorithm to

relax all ionic positions until the tolerance in total energy was lower than 0.0001 eV between two ionic steps during geometrical optimizations. The *k*-points were set as 3 × 3 × 1 and then changed to 7 × 7 × 1 in the electronic structure calculation stage by using a Monkhorst-Pack grid. A vacuum layer of 15 Å along the *Z*-axis was tested to be enough and was chosen to avoid periodic layer interactions.

RESULTS AND DISCUSSION

Fig. 1a illustrates the preparation process of N/P-HMCNs *via* a hard-template method. Typically, aniline monomers were initially polymerized in the presence of phytic acid and colloidal silica nanoparticles to produce silica-PANi core-shell composite nanospheres that were pyrolyzed and subsequently etched by dilute HF acid to obtain N/P-HMCNs. For comparison, ordered N-HMCNs without phosphorous doping were prepared (details are discussed in the EXPERIMENTAL SECTION). SEM and TEM images show that N/P-HMCNs have a uniformly spherical morphology (Fig. 1b, c). The average size of N/P-HMCNs is ~175 nm, which is smaller than that of the silica-PANi core-shell composite nanospheres (~197 nm, Fig. S1), suggesting the shrinkage caused by PANi decomposition during pyrolysis. TEM images in Fig. 1c, d show that N/P-HMCNs have an ordered mesoporous structure with a pore diameter of around 9 nm. The mesopores on N/P-HMCNs are spherical, which originate from the removal of Si nanoparticle templates (Fig. S1). High-resolution TEM (HRTEM) images in Fig. 1d, e further reveal that the ordered mesopores are separated by interconnected, highly curved, atom-thick pore walls. Energy-dispersive X-ray spectroscopy (EDS) mappings (Fig. 1f, g) confirm the uniform doping of N and P over the entire N/P-HMCNs, which is related to the *in situ* polymerization between aniline and phytic acid. The morphology and structure of N-HMCNs (Fig. S2) are similar to those of N/P-HMCNs.

XRD patterns (Fig. 2a) of the as-prepared N/P-HMCNs and N-HMCNs show broad peaks at around 22° and 43°, corresponding to the characteristic peaks of graphitic carbon (002) and (100) diffraction, respectively. The broadened XRD peaks imply the poor crystallinity and low degree of graphitization of the as-prepared carbon samples, which is consistent with the above-mentioned HRTEM results. The average intergraphene layer spacings (d_{002}) for N/P-HMCNs and N-HMCNs are calculated as ~0.40 and 0.41 nm, respectively, suggesting an expanded graphene-layer structure of the as-prepared carbon materials. Raman spectroscopy was further used to evaluate the quality of the as-prepared carbon materials. As shown in Fig. 2b and Fig. S3, two broad peaks are found around 1350 and 1590 cm^{-1} in the Raman spectra, which can be assigned to disorder-induced D-band and in-plane vibration G-band of carbon [29]. The relative intensity (I_D/I_G) ratios for N/P-HMCNs and N-HMCNs are 1.0 and 0.96, respectively. The low I_D/I_G values for N/P-HMCNs and N-HMCNs may be related to their highly porous structure, curved pore walls, and high heteroatom doping level. The nitrogen gas adsorption and desorption isotherms of N/P-HMCNs and N-HMCNs feature a hysteresis loop (type IV). The pore size distribution curve (Fig. 2d) for N/P-HMCNs, which is calculated using a nonlocal DFT, confirms the formation of mesopores mainly centered at 10 nm and micropores mainly centered at 1.6 nm. The mesopores of N/P-HMCNs account for more than 66% of their pore volume (Table S1). A slight difference in the pore size distribution between N/P-HMCNs and N-HMCNs may be related to the unique crosslink structure between phytic acid and PANi. In some cases, PANi hydrogel is formed with a suitable amount of phytic acid and PANi mass ratio can be transformed into a meso–microporous carbon after pyrolysis. On the other hand, nonporous carbon is formed without phytic acid [30]. The Brunauer-Emmett-Teller (BET) specific surface area and pore volume of N/P-HMCNs are 869.64 $m^2 g^{-1}$ and 1.92 $cm^3 g^{-1}$, respectively, whereas N-HMCNs show an increased BET specific surface area of 946.28 $m^2 g^{-1}$ and a reduced pore volume of 1.51 $cm^3 g^{-1}$, respectively.

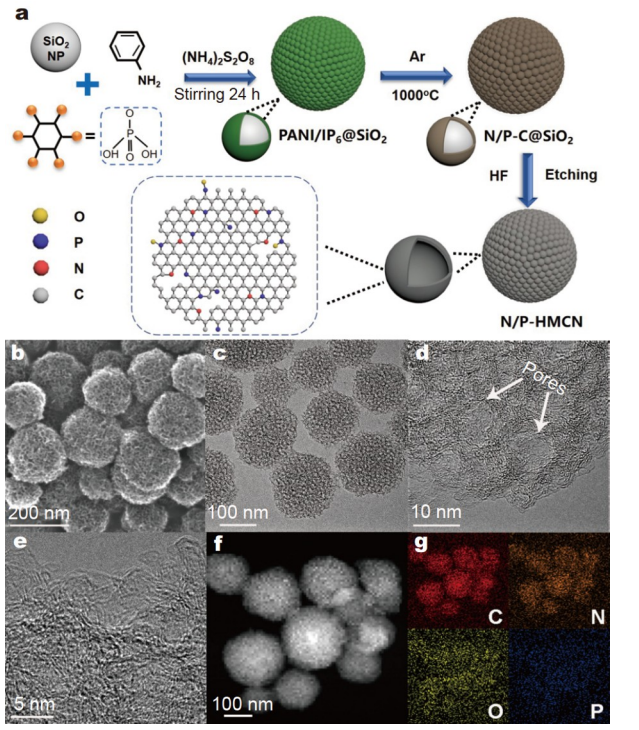

Figure 1 (a) Typical synthesis procedure of N/P-HMCNs. (b) SEM image of N/P-HMCNs, (c–e) TEM images of N/P-HMCNs, and (f) high-angle annular dark field-scanning TEM (HAADF-STEM) image as well as (g) EDS mappings of C, N, O, and P.

XPS measurements were employed to further investigate the surface element components and chemical state of the as-prepared samples. The overall XPS spectra (Fig. S4a) of N/P-HMCNs show peaks for C, N, O, and P, whereas the peak for P is not detected in N-HMCNs. The N, O, and P heteroatom contents of N/P-HMCNs are 3.99, 12.32, and 3.04 at%, respectively (Table S1). The increased O and P contents are observed in N/P-HMCNs but not in N-HMCNs, which arise mainly from the phytic acid precursor. The C 1s spectra of N/P-HMCNs and N-HMCNs (Fig. S4b) can be deconvoluted into four peaks: C–C, C–O, C=O, and O–C=O. The O 1s spectra of N/P-HMCNs and N-HMCNs (Fig. S4c) can be deconvoluted into three peaks centered at 530.1, 532.7, and 535.5 eV, which are assigned to C=O quinone groups (O-I), C–OH hydroxyl groups or C–O–C ether groups (O-II), and –O–C=O carboxyl groups (O-III), respectively. The HR spectrum of N 1s of N/P-HMCNs (Fig. 2e) could be well deconvoluted into four different bands, corresponding to pyridine-N (N-6 at a binding energy (BE) of 398.8 eV), pyrrole-N (N-5 at BE = 400.8 eV), graphitic-N (N-Q at BE = 401.3 eV), and oxidized-N (N-X at BE = 402.5 eV),

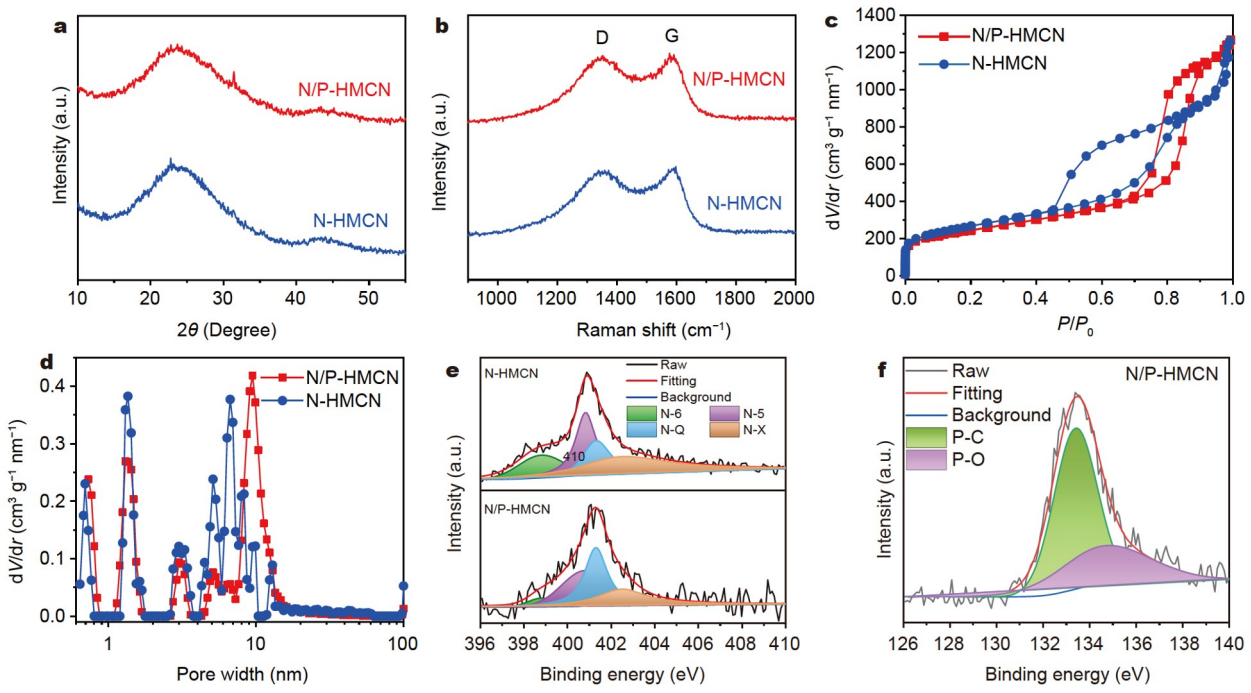

Figure 2 (a) XRD patterns, (b) Raman spectra, (c) nitrogen adsorbed-desorbed isotherms, (d) pore size distribution curves of N/P-HMCN and N-HMCN. (e) N 1s XPS spectra of N/P-HMCNs and N-HMCNs. (f) P 2p XPS spectrum of N/P-HMCNs.

respectively [31]. The high proportion of N-Q in N/P-HMCNs suggests that graphitic-N is the prevailing form of nitrogen in N/P-HMCNs, which is also observed in N-HMCNs. The HR P 2p spectrum of N/P-HMCNs (Fig. 2f) was deconvoluted into two different bands at 133.4 and 134.6 eV, corresponding to the P atoms in the P–C and P–O bonds, respectively [32]. The formation of the P–C bond enhances the adsorption capacity of the graphite layer for Li^+, thus improving the specific capacity of Li^+ charge storage [33]. These various nitrogen and phosphorous species on the carbon matrix result in different chemical and electronic environments for neighboring carbon atoms and hence different electrochemical activities for Li^+ charge storage [34].

To evaluate the electrochemical performance of the as-prepared carbon anodes, half cells *versus* Li metal electrodes were employed. Fig. 3a shows the CV curves of the N/P-HMCN electrode at a sweep rate of 0.2 mV s^{-1} with a voltage range of 0.01–3.00 V (*versus* Li^+/Li). In the first lithiation cycle, there is an obvious cathodic peak at around 0.54 V (*versus* Li^+/Li), which is related to the simultaneous production of a solid electrolyte interface (SEI) layer and the irreversible side reactions between the electrolyte and surface functional groups [17,35,36]. As the potential falls below 0.3 V (*versus* Li^+/Li), the cathodic current density continuously increases, which is due to the synergistic effect of continuous Li^+ intercalation into the carbon layer and irreversible side effects arising from the reaction between the electrolyte and surface functional groups and the SEI formation. In the subsequent anodic process, an approximately linear polarization curve parallel to the horizontal axis without obvious peaks appears, indicating the multiple charge storage mechanisms combined with stepwise insertion/desertion of Li^+ from the carbon matrix and the homogeneous reversible reactions between Li^+ and surface functional groups depending on voltage [37]. During the succeeding cycles, the CV curves tend to overlap, indicating the high reversibility of the lithiation-delithiation process.

To probe the reaction kinetics during lithium-ion charge storage on the as-prepared N/P-HMCNs, CV experiments at various scan rates from 0.2 to 100 mV s^{-1} were carried out (Fig. S5a, b). These CV curves feature similar profiles without obvious redox peaks, indicating that N/P-HMCNs have many easily accessible surface-redox active sites resulting from their highly porous structure and abundant functional groups. The *b* values (appropriate value to evaluate pseudocapacitive behavior) are calculated to be 0.89 (Fig. S5c), when the CV scan rates are in the range of 0.2–10 mV s^{-1}, indicating that the redox reaction is predominately surface-controlled (or capacitive-dominated). The capacitive contribution to the current response can be further quantified. As illustrated in Fig. S5d, e, the pseudocapacitive current response accounts for 56% of the total measured current response at a sweep rate of 1 mV s^{-1}. These results suggest that the rich N/P co-dopants and porous structure provide more surface defects that could promote Li^+ storage and thus result in fast reaction kinetics.

Fig. S6 shows the initial charge-discharge curves of N/P-HMCNs and N-HMCNs at a current density of 0.1 A g^{-1}. The N/P-HMCN and N-HMCN electrodes deliver reversible specific capacities of 989.0 and 786.3 mA h g^{-1} with the initial Coulombic efficiencies of 43.5% and 41.2%, respectively. The irreversible capacity is mainly caused by the formation of the SEI layer and irreversible reactions between Li^+ and surface functional groups [38], which is consistent with CVs. The low initial Coulombic efficiency could be alleviated through prelithiation techniques and electrolyte additives [39]. The specific capacities for these carbon anodes decrease slowly in the subsequent cycles, indicating their enhanced and highly reversible lithiated-delithiated properties. Except for the initial cycles, the charge-discharge curves at a current density of 0.1 A g^{-1} plotted in Fig. S6

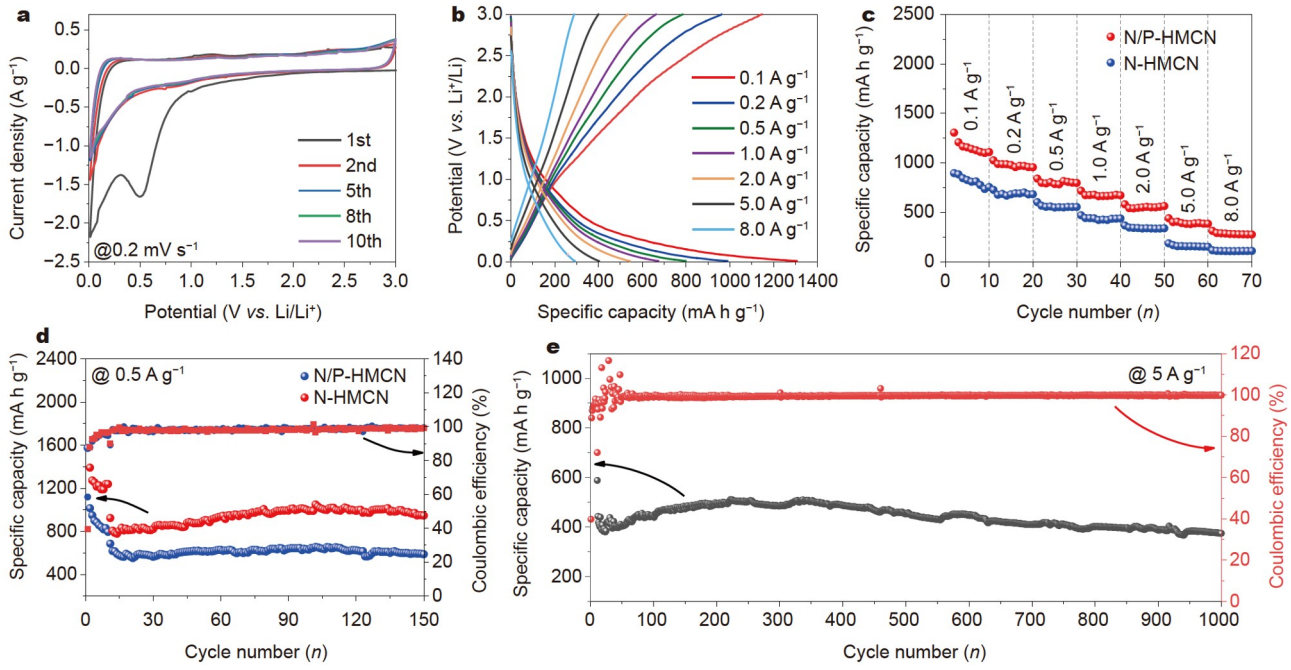

Figure 3 Li^+ storage behavior of the N/P-HMCN anode in a half cell within an operating potential range of 0.01–3.00 V (*versus* Li/Li^+). (a) Initial CV curves at 0.2 mV s^{-1}. (b) Charging-discharging curves at different current densities. (c) Rate capability results. Cycling performance at (d) 0.5 A g^{-1} and (e) 5 A g^{-1} (initial 10 cycles worked at 0.1 A g^{-1}).

feature a sloped profile without a voltage plateau within 0.01–3.00 V (*versus* Li/Li^+), which is a common characteristic found in porous carbons and heteroatom-doped carbons [20,40–42]. Similar sloped profiles are also observed in the charge-discharge curves under gradually elevated current densities, as shown in Fig. 3b.

The rate capabilities of the as-prepared carbon anodes were evaluated at different current densities from 0.1 to 8 A g^{-1}. The results plotted in Fig. 3c show that N/P-HMCNs deliver reversible capacities of 1108.6, 955.9, 797.4, 672.2, 563.7, and 384.7 mA h g^{-1} at the current densities of 0.1, 0.2, 0.5, 1, 2, and 5 A g^{-1}, respectively. Even when the current density increases to 8 A g^{-1}, a reversible capacity of 276.5 mA h g^{-1} can be maintained, indicating a good rate capability. In comparison with N/P-HMCNs, N-HMCNs lack the electroactive phosphorous functional groups, yielding lower specific capacities of 755.4 mA h g^{-1} at 0.1 A g^{-1} and 110.6 mA h g^{-1} at 8 A g^{-1}. Since both N/P-HMCNs and N-HMCNs have similar porous structures and nitrogen doping levels, it is reasonable to speculate that phosphorus doping plays an important role in providing additional Li^+ charge storage sites for N/P-HMCNs.

The cycling performance of the as-prepared carbon anodes at different current densities was evaluated. The N/P-HMCN anode showed no decay with a reversible capacity of 946.2 mA h g^{-1} at 0.5 A g^{-1} after 150 cycles (Fig. 3d) and a reversible capacity of 666.9 mA h g^{-1} at 2 A g^{-1} after 250 cycles (Fig. S7), which are higher than those based on N-HMCNs. Even at a high current density of 5 A g^{-1}, the N/P-HMCN anode still preserves a highly reversible capacity of 374.5 mA h g^{-1} after 1000 cycles, corresponding to a capacity retention value of 85% (Fig. 3e). During the whole cycling test, the Coulombic efficiency of N/P-HMCNs is approximately 100%.

To further probe the structural merits of N/P-HMCNs, several comprehensive methods were employed to analyze the structure evolution and interface change during the electrochemical process. Fig. 4a shows the *ex situ* Raman spectra of the N/P-HMCN anode obtained at the initial and delithiated states after ten cycles as well as at the delithiated state after 1000 cycles. D and G peaks show no apparent change after cycling relative to the initial state, revealing highly reversible processes with no structural change during long cycles. Fig. S8 displays the full XPS spectra of N/P-HMCNs at different cycling states. After the cycles, the N 1s disappears and new peaks of F 1s appear, which is mainly caused by the formation of the SEI layer on the surface of N/P-HMCNs. The HR C 1s XPS spectrum shown in Fig. 4b and the main peak around 284.7 eV assigned to C–C species show no shift, confirming the stable structure of N/P-HMCNs during cycling. The enhanced peaks at around 286.5 and 289.9 eV after ten cycles can be assigned to the C–O and RO–COOLi groups, respectively, mainly stemming from the decomposition of electrolyte and SEI layer formation [43–45]. The HR O 1s XPS spectrum shown in Fig. S9a further confirms the formation of Li salt, RO–COOLi, and RO–Li. Meanwhile, LiF/Li_xPF_y signals are detected throughout the whole cycling process (Fig. 4c and Fig. S9b). These results suggest that the top surface of the SEI layer consists of both organic (RO–COOLi/RO–Li) and inorganic (Li_2CO_3 and LiF) components. Furthermore, little change for C 1s, O 1s, P 2p, and F 1s occurs after the long cycles, suggesting the structural stability of the N/P-HMCN anode and SEI layer. The TEM characterization with EDS mappings shown in Fig. S10 further confirms that N/P-HMCNs still preserve the nanosphere morphology covered with the SEI layer after long cycles.

In order to further reveal the intrinsic reasons for the improvement of the electrochemical properties of the N/P-HMCN anode by nitrogen and phosphorus co-doping, DFT calculations were carried out. According to XPS results, we established five regularly repeated carbon laboratory models for

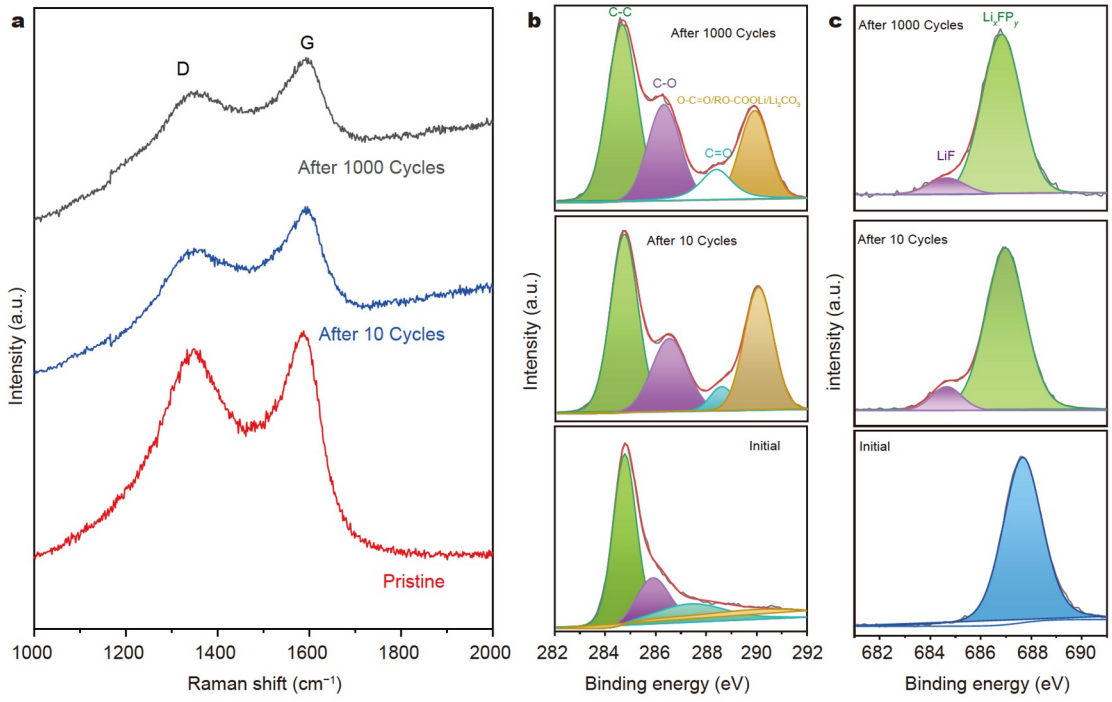

Figure 4 (a) Raman spectra of the N/P-HMCN anode at different cycling states. Chemical component analyses of the SEI layer at different potentials *via* (b) C 1s and (c) F 1s XPS at different states, including initial state, after ten cycles, and after 1000 cycles.

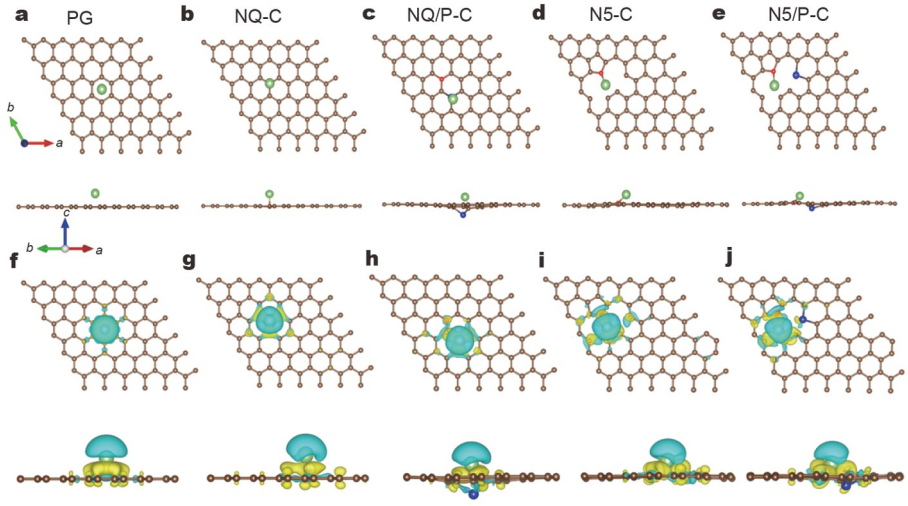

Figure 5 Five calculation models after Li^+ adsorption on (a) PG, (b) NQ-C, (c) NQ/P-C, (d) N5-C and (e) N5/P-C. (f–j) Charge density diagram of various models. The iso-surface level = 0.0015 e $Bohr^{-3}$. The yellow areas represent charge accumulation, the cyan areas represent charge depletion, and the brown, red, blue, and green balls represent C, N, P, and Li atoms, respectively.

systematic study, namely, pure graphene (PG, Fig. 5a), graphite nitrogen-doped carbon (NQ-C, Fig. 5b), graphite nitrogen- and phosphorus-doped carbon (NQ/P-C, Fig. 5c), pyridine nitrogen-doped carbon (N5-C, Fig. 5d), and pyridine nitrogen- and phosphorus-doped carbon (N5/P-C, Fig. 5e). We used graphene to represent the structure of the carbon system. When Li^+ ions are adsorbed in these systems, the most stable electronic structures are obtained. In addition, their adsorption energy (ΔE_{ad}) can be calculated by the following formula:

$$\Delta E_{ad} = E_{Li+sub} - E_{sub} - E_{Li}, \quad (3)$$

where E_{Li+sub} represents the total energy of the system with Li adsorbed on the carbon substrate, and E_{sub} and E_{Li} represent the total energy of an isolated carbon system and Li atoms, respectively. As shown in Table S2, ΔE_{ad} of PG, NQ-C, NQ/P-C, N5-C, and N5/P-C is 0.483, 1.204, −1.602, −0.775, and −1.784 eV, respectively. This indicates that N/P co-doping can significantly increase the adsorption capacity of carbon materials to Li^+ because this type of doping can increase the active sites and provide additional defects, thus improving the adsorption energy [17]. The calculated results of the adsorption energy combined with the charge density diagram (Fig. 5f–j) show that N/P co-doping could effectively change the electronic structure

of carbon atoms and the charge distribution around the Li atom, thus promoting Li-adsorption ability. Overall, these results from electrochemical and structural characterizations, as well as theoretical calculations, demonstrate that N/P-HMCNs with highly meso–microporous structure and N/P co-doped properties account for the excellent electrochemical performance with respect to high specific capacity, acceptable rate capability, and robust cycle stability.

To demonstrate the potential of N/P-HMCNs as a high-performance anode for emerging energy-storage devices, full-cell LICs using N/P-HMCNs as an anode and the as-prepared PDPC as a cathode in $LiPF_6$-based organic electrolyte were fabricated, as schematically illustrated in Fig. 6a. More details on the PDPC cathode can be seen in our previous work [46,47]. The mass ratio between the anode and cathode was optimized to 1:1 to reduce polarization and maximize electrochemical performance, including energy and power densities and cycle stability (Figs S11 and S12). To further understand the respective electrochemical behavior of the cathode and anode, a three-electrode Swagelok cell with Li metal as an auxiliary electrode was assembled. Fig. 6b shows the CV curves of a voltage window of 1.0–4.0 V for the full cell (red) and single electrode (green cathode and purple cathode) at a scan rate of 50 mV s^{-1}. The CV curve of N/P-HMCNs//PDPC LIC exhibits a quasirectangular shape, which is associated with the synergetic effect between the battery-like N/P-HMCN anode and double-layer capacitive PDPC cathode. The anode operating potential of N/P-HMCNs is in the range of 0.36–1.06 V against Li/Li^+, whereas that of the PDPC cathode is in the range of 2.15–4.38 V against Li/Li^+ (Fig. 6b). As the scan rate increases up to 200 mV s^{-1} (Fig. S13), the CV curve still features a near-rectangular profile, which indicates the capacitive properties and excellent rate capability of the as-fabricated LIC. Under such a high scan rate, the operating potential ranges of the anode and cathode are still in the stable

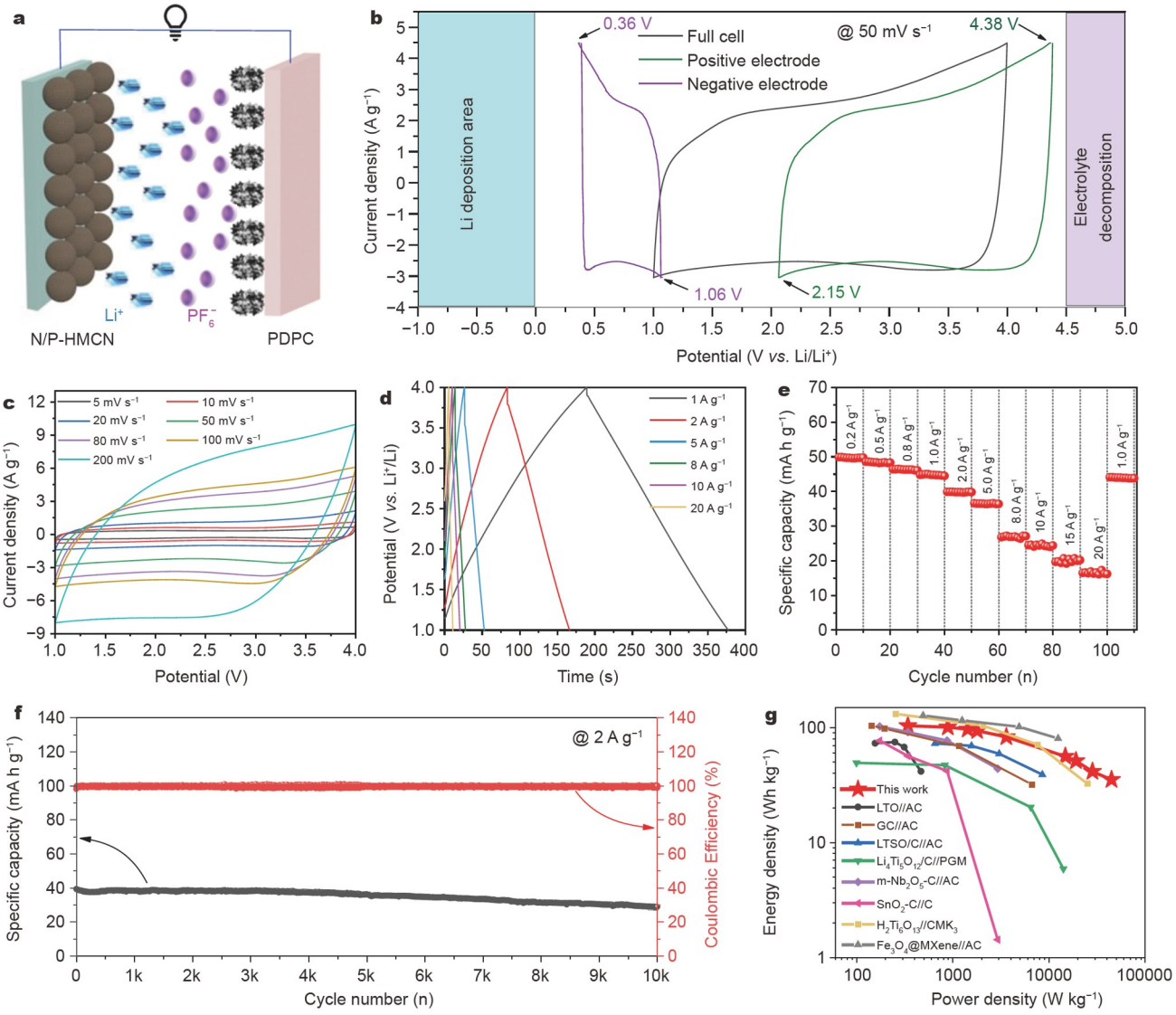

Figure 6 Capacity performance of the N/P-HMCNs//PDPC LIC in full-cell configuration. (a) Schematic image of the assembled full-cell device. (b) CV profile based on a three-electrode device at 50 mV s^{-1}. (c) CV profile at different scan rates. (d) Charging-discharging curves at different current densities. (e) Specific capacities at different discharging current densities. (f) Long-term cycling performance at 2 A g^{-1}. (g) Ragone plots showing the energy and power densities of the as-fabricated LIC *versus* those of LICs reported.

region, which confirms the absence of electrolyte decomposition or Li plating.

Fig. 6d and Fig. S14 show the charging-discharging curves of N/P-HMCNs//PDPC LIC at different current densities. All these curves exhibit an approximately linear slope, further confirming the good capacitive properties of the as-fabricated LIC. The specific capacity values of N/P-HMCNs//PDPC LIC (based on the total mass of anodic and cathodic active materials) are 49.7, 48.4, 46.4, 45.0, 39.8, 36.5, 26.9, and 24.6 mA h g^{-1} at the current densities of 0.2, 0.5, 0.8, 1.0, 2.0, 5.0, 8.0, and 10.0 A g^{-1}, respectively, as shown in Fig. 6e. Even at an extremely high current density of 20.0 A g^{-1}, the as-fabricated LIC still yields a specific capacity of 16.9 mA h g^{-1}.

We also used the Swagelok cell to monitor the potential swings of the anode and cathode in the full cell under different charge-discharge rates (Fig. S15). As the current density increases from 0.2 to 20 A g^{-1}, the respective working potential windows for the anode and cathode are in the safe area, avoiding side reactions caused by Li plating and electrolyte decomposition. This is also beneficial to the stability of long cycles. As shown in Fig. 6f, N/P-HMCNs//PDPC LIC exhibits robust cycle stability with a capacitance retention ratio of ~85% after 10,000 cycles at a current density of 2 A g^{-1}. The Coulombic efficiency of N/P-HMCNs//PDPC LIC is nearly 100% during the whole cycling. The capacity decay of the as-fabricated LIC is mainly caused by the increased SEI resistance and the step-down Li^+ diffusion after long cycles, as suggested by the EIS results (Fig. S16). The energy density and power density of N/P-HMCNs//PDPC LIC were further evaluated, as plotted in Fig. 6g. With a power density of 341 W kg^{-1}, the as-fabricated LIC offers a high energy density of 103 W h kg^{-1}. Even at an ultrahigh power density of over 44,630 W kg^{-1}, it can still deliver an energy density of 35 W h kg^{-1}. The Ragone plots in Fig. 6g show that the energy and power densities of the as-fabricated LIC are highly comparable or even exceeded those of many LICs that have been reported (Table S3), including $Li_4Ti_5O_{12}$(LTO)//AC [48], $Li_4Ti_5O_{12}$/C//porous graphene macroform (PGM)[49], graphitic carbon (GC)//AC [50], Li_2TiSiO_5(LTSO)/C//AC [51], m-Nb_2O_5-C//AC [52], SnO_2-C//C [53], $H_2Ti_6O_{13}$//CMK-3 [54], Fe_3O_4/C@MXenes//AC [55], Fe_2TiO_5/super conducting carbon black (SCCB)[56], N-doped carbon//AC [57], $TiNb_2O_7$//AC [58], $Ti_3C_2T_x$/rGO//AC [59], and soft carbon (SC)//AC [60].

CONCLUSIONS

In summary, we developed an approach to improve the energy and power densities of the as-fabricated LIC by optimizing the structure of the carbon anode materials. The carbon anode is synthesized by pyrolyzing silica-PANi core-shell composite nanospheres obtained through template polymerization of aniline in the presence of phytic acid and shows a uniformly spherical morphology with a hierarchical meso–microporous structure and nitrogen/phosphorous co-doped properties. Owing to their unique structure characteristics, the resultant N/P-HMCNs exhibit a highly reversible specific capacity of 1108.6 mA h g^{-1} at 0.1 A g^{-1} with an excellent rate capability (276.5 mA h g^{-1} at 8 A g^{-1}) and long-term cycle stability (exceeding 1000 cycles). As a proof-of-concept application, the as-fabricated full-cell LIC based on the N/P-HMCN anode delivers an energy density of 103 W h kg^{-1} at 341 W kg^{-1} and remains 35 W h kg^{-1} even at a high power density of 44,630 W kg^{-1} as well as long cycle life (87.5% after 10,000 cycles). Hence, this work provides an essential reference for the structural control of carbon materials at the nano/atomic scale with synergistic electrochemical merits.

Received 22 December 2021; accepted 22 March 2022; published online 8 June 2022

1 Jeżowski P, Crosnier O, Deunf E, *et al.* Safe and recyclable lithium-ion capacitors using sacrificial organic lithium salt. Nat Mater, 2018, 17: 167–173
2 Simon P, Gogotsi Y. Perspectives for electrochemical capacitors and related devices. Nat Mater, 2020, 19: 1151–1163
3 Liu W, Zhang X, Xu Y, *et al.* Recent advances on carbon-based materials for high performance lithium-ion capacitors. Batteries Supercaps, 2021, 4: 407–428
4 Li T, Zhao H, Li C, *et al.* Recent progress and prospects in anode materials for potassium-ion capacitors. New Carbon Mater, 2021, 36: 253–277
5 Ajuria J, Redondo E, Arnaiz M, *et al.* Lithium and sodium ion capacitors with high energy and power densities based on carbons from recycled olive pits. J Power Sources, 2017, 359: 17–26
6 Kim JH, Kim JS, Lim YG, *et al.* Effect of carbon types on the electrochemical properties of negative electrodes for Li-ion capacitors. J Power Sources, 2011, 196: 10490–10495
7 Li C, Zhang X, Wang K, *et al.* High-power lithium-ion hybrid supercapacitor enabled by holey carbon nanolayers with targeted porosity. J Power Sources, 2018, 400: 468–477
8 Xie L, Tang C, Bi Z, *et al.* Hard carbon anodes for next-generation Li-ion batteries: Review and perspective. Adv Energy Mater, 2021, 11: 2101650
9 Zhang LL, Zhao XS. Carbon-based materials as supercapacitor electrodes. Chem Soc Rev, 2009, 38: 2520–2531
10 Ma Y, Chang H, Zhang M, *et al.* Graphene-based materials for lithium-ion hybrid supercapacitors. Adv Mater, 2015, 27: 5296–5308
11 Han P, Xu G, Han X, *et al.* Lithium ion capacitors in organic electrolyte system: Scientific problems, material development, and key technologies. Adv Energy Mater, 2018, 8: 1801243
12 Zheng JS, Zhang L, Shellikeri A, *et al.* A hybrid electrochemical device based on a synergetic inner combination of Li ion battery and Li ion capacitor for energy storage. Sci Rep, 2017, 7: 41910
13 Liu T, Zhang L, Cheng B, *et al.* Hollow carbon spheres and their hybrid nanomaterials in electrochemical energy storage. Adv Energy Mater, 2019, 9: 1803900
14 Xu F, Tang Z, Huang S, *et al.* Facile synthesis of ultrahigh-surface-area hollow carbon nanospheres for enhanced adsorption and energy storage. Nat Commun, 2015, 6: 7221
15 Li B, Zheng J, Zhang H, *et al.* Electrode materials, electrolytes, and challenges in nonaqueous lithium-ion capacitors. Adv Mater, 2018, 30: 1705670
16 Liu M, Zhang Z, Dou M, *et al.* Nitrogen and oxygen co-doped porous carbon nanosheets as high-rate and long-lifetime anode materials for high-performance Li-ion capacitors. Carbon, 2019, 151: 28–35
17 Jiang J, Zhang Y, Li Z, *et al.* Defect-rich and N-doped hard carbon as a sustainable anode for high-energy lithium-ion capacitors. J Colloid Interface Sci, 2020, 567: 75–83
18 Li C, Zhang X, Wang K, *et al.* High-power and long-life lithium-ion capacitors constructed from N-doped hierarchical carbon nanolayer cathode and mesoporous graphene anode. Carbon, 2018, 140: 237–248
19 Jia QC, Zhang HJ, Kong LB. Nanostructure-modified *in-situ* synthesis of nitrogen-doped porous carbon microspheres (NPCM) loaded with $FeTe_2$ nanocrystals and NPCM as superior anodes to construct high-performance lithium-ion capacitors. Electrochim Acta, 2020, 337: 135749
20 Zou K, Guan Z, Deng Y, *et al.* Nitrogen-rich porous carbon in ultrahigh yield derived from activation of biomass waste by a novel eutectic salt for high performance Li-ion capacitors. Carbon, 2020, 161: 25–35
21 Yang C, Ren J, Zheng M, *et al.* High-level N/P co-doped Sn-carbon nanofibers with ultrahigh pseudocapacitance for high-energy lithium-ion and sodium-ion capacitors. Electrochim Acta, 2020, 359: 136898

22 Luan Y, Hu R, Fang Y, *et al.* Nitrogen and phosphorus dual-doped multilayer graphene as universal anode for full carbon-based lithium and potassium ion capacitors. Nano-Micro Lett, 2019, 11: 30
23 Shao D, Tang D, Yang J, *et al.* Nano-structured composite of Si/(S-doped-carbon nanowire network) as anode material for lithium-ion batteries. J Power Sources, 2015, 297: 344–350
24 Shao D, Smolianova I, Tang D, *et al.* Novel core-shell structured Si/S-doped-carbon composite with buffering voids as high performance anode for Li-ion batteries. RSC Adv, 2017, 7: 2407–2414
25 Sun Y, Wang H, Wei W, *et al.* Sulfur-rich graphene nanoboxes with ultra-high potassiation capacity at fast charge: Storage mechanisms and device performance. ACS Nano, 2021, 15: 1652–1665
26 Xia Q, Yang H, Wang M, *et al.* High energy and high power lithium-ion capacitors based on boron and nitrogen dual-doped 3D carbon nanofibers as both cathode and anode. Adv Energy Mater, 2017, 7: 1701336
27 Zhao G, Li Y, Zhu G, *et al.* Biomass-based N, P, and S self-doped porous carbon for high-performance supercapacitors. ACS Sustain Chem Eng, 2019, 7: 12052–12060
28 Panja T, Bhattacharjya D, Yu JS. Nitrogen and phosphorus co-doped cubic ordered mesoporous carbon as a supercapacitor electrode material with extraordinary cyclic stability. J Mater Chem A, 2015, 3: 18001–18009
29 Nemanich RJ, Solin SA. First- and second-order Raman scattering from finite-size crystals of graphite. Phys Rev B, 1979, 20: 392–401
30 Zhang J, Zhao Z, Xia Z, *et al.* A metal-free bifunctional electrocatalyst for oxygen reduction and oxygen evolution reactions. Nat Nanotech, 2015, 10: 444–452
31 Ding J, Li Z, Cui K, *et al.* Heteroatom enhanced sodium ion capacity and rate capability in a hydrogel derived carbon give record performance in a hybrid ion capacitor. Nano Energy, 2016, 23: 129–137
32 Qian Y, Jiang S, Li Y, *et al. In situ* revealing the electroactivity of P–O and P–C bonds in hard carbon for high-capacity and long-life Li/K-ion batteries. Adv Energy Mater, 2019, 9: 1901676
33 Yang C, Zhang M, Kong N, *et al.* Self-supported carbon nanofiber films with high-level nitrogen and phosphorus co-doping for advanced lithium-ion and sodium-ion capacitors. ACS Sustain Chem Eng, 2019, 7: 9291–9300
34 Bi Z, Kong Q, Cao Y, *et al.* Biomass-derived porous carbon materials with different dimensions for supercapacitor electrodes: A review. J Mater Chem A, 2019, 7: 16028–16045
35 Lin YX, Liu Z, Leung K, *et al.* Connecting the irreversible capacity loss in Li-ion batteries with the electronic insulating properties of solid electrolyte interphase (SEI) components. J Power Sources, 2016, 309: 221–230
36 Song MX, Xie LJ, Cheng JY, *et al.* Insights into the thermochemical evolution of maleic anhydride-initiated esterified starch to construct hard carbon microspheres for lithium-ion batteries. J Energy Chem, 2022, 66: 448–458
37 Zhou X, Chen L, Zhang W, *et al.* Three-dimensional ordered macroporous metal-organic framework single crystal-derived nitrogen-doped hierarchical porous carbon for high-performance potassium-ion batteries. Nano Lett, 2019, 19: 4965–4973
38 Soto FA, Yan P, Engelhard MH, *et al.* Tuning the solid electrolyte interphase for selective Li- and Na-ion storage in hard carbon. Adv Mater, 2017, 29: 1606860
39 Wang F, Wang B, Li J, *et al.* Prelithiation: A crucial strategy for boosting the practical application of next-generation lithium ion battery. ACS Nano, 2021, 15: 2197–2218
40 Jiang J, Yuan J, Nie P, *et al.* Hierarchical N-doped hollow carbon microspheres as advanced materials for high-performance lithium-ion capacitors. J Mater Chem A, 2020, 8: 3956–3966
41 Xu Y, Jiang J, Li Z, *et al.* Aerosol-assisted preparation of N-doped hierarchical porous carbon spheres cathodes toward high-stable lithium-ion capacitors. J Mater Sci, 2020, 55: 13127–13140
42 Yan D, Zhang J, Xiong D, *et al.* Boosting chem-insertion and physadsorption in S/N co-doped porous carbon nanospheres for high-performance symmetric Li-ion capacitors. J Mater Chem A, 2020, 8: 11529–11537
43 Chen J, Fan X, Li Q, *et al.* Electrolyte design for LiF-rich solid-electrolyte interfaces to enable high-performance microsized alloy anodes for batteries. Nat Energy, 2020, 5: 386–397
44 Liu W, Chen Z, Zhang Z, *et al.* Lithium-activated SnS-graphene alternating nanolayers enable dendrite-free cycling of thin sodium metal anodes in carbonate electrolyte. Energy Environ Sci, 2021, 14: 382–395
45 Liu T, Lin L, Bi X, *et al. In situ* quantification of interphasial chemistry in Li-ion battery. Nat Nanotech, 2019, 14: 50–56
46 Wang R, Wang S, Jin D, *et al.* Engineering layer structure of MoS_2-graphene composites with robust and fast lithium storage for high-performance Li-ion capacitors. Energy Storage Mater, 2017, 9: 195–205
47 Bian Y, Wang S, Jin D, *et al.* A general anion exchange strategy to transform metal-organic framework embedded nanofibers into high-performance lithium-ion capacitors. Nano Energy, 2020, 75: 104935
48 Amatucci GG, Badway F, Du Pasquier A, *et al.* An asymmetric hybrid nonaqueous energy storage cell. J Electrochem Soc, 2001, 148: A930
49 Ye L, Liang Q, Lei Y, *et al.* A high performance Li-ion capacitor constructed with $Li_4Ti_5O_{12}$/C hybrid and porous graphene macroform. J Power Sources, 2015, 282: 174–178
50 Yang Z, Guo H, Li X, *et al.* Graphitic carbon balanced between high plateau capacity and high rate capability for lithium ion capacitors. J Mater Chem A, 2017, 5: 15302–15309
51 Wang S, Wang R, Bian Y, *et al. In-situ* encapsulation of pseudocapacitive Li_2TiSiO_5 nanoparticles into fibrous carbon framework for ultrafast and stable lithium storage. Nano Energy, 2019, 55: 173–181
52 Lim E, Kim H, Jo C, *et al.* Advanced hybrid supercapacitor based on a mesoporous niobium pentoxide/carbon as high-performance anode. ACS Nano, 2014, 8: 8968–8978
53 Qu WH, Han F, Lu AH, *et al.* Combination of a SnO_2-C hybrid anode and a tubular mesoporous carbon cathode in a high energy density non-aqueous lithium ion capacitor: Preparation and characterisation. J Mater Chem A, 2014, 2: 6549–6557
54 Wang Y, Hong Z, Wei M, *et al.* Layered $H_2Ti_6O_{13}$-nanowires: A new promising pseudocapacitive material in non-aqueous electrolyte. Adv Funct Mater, 2012, 22: 5185–5193
55 Wang S, Jin D, Bian Y, *et al.* Electrostatically fabricated three-dimensional magnetite and MXene hierarchical architecture for advanced lithium-ion capacitors. ACS Appl Mater Interfaces, 2020, 12: 9226–9235
56 Kang R, Zhu WQ, Li S, *et al.* Fe_2TiO_5 nanochains as anode for high-performance lithium-ion capacitor. Rare Met, 2021, 40: 2424–2431
57 Zhou J, Xu S, Kang Q, *et al.* Iron oxide encapsulated in nitrogen-rich carbon enabling high-performance lithium-ion capacitor. Sci China Mater, 2020, 63: 2289–2302
58 Deng B, Dong H, Lei T, *et al.* Post-annealing tailored 3D cross-linked $TiNb_2O_7$ nanorod electrode: Towards superior lithium storage for flexible lithium-ion capacitors. Sci China Mater, 2020, 63: 492–504
59 Yi S, Wang L, Zhang X, *et al.* Cationic intermediates assisted self-assembly two-dimensional Ti_3C_2T/rGO hybrid nanoflakes for advanced lithium-ion capacitors. Sci Bull, 2021, 66: 914–924
60 Sun C, Zhang X, Li C, *et al.* High-efficiency sacrificial prelithiation of lithium-ion capacitors with superior energy-storage performance. Energy Storage Mater, 2020, 24: 160–166

Acknowledgements This work was supported by the National Natural Science Foundation of China (51902188, 21603125, and 52171182), the Natural Science Foundation of Jiangsu Province (BK20190207), the CAS Key Laboratory of Carbon Materials (KLCMKFJJ2006), and the Key Research and Development Program of Shandong Province (2021ZLGX01). The authors are grateful for the computational support from the National Supercomputer Centre (NSC), the HPC Cloud Platform of Shandong University, and the Young Scholars Program of Shangdong University.

Author contributions Li T, Wang R, Zhang J, Qian Z, and Yin L designed and engineered the samples; Li T, Zhang J, Li C, and Zhao H performed the experiments; Li T and Zhang J wrote the paper with the support from Wang R, Zhang J, Qian Z, and Yin L. All authors contributed to the general discussion.

Conflict of interest The authors declare that they have no conflict of interest.

Supplementary information Supporting data are available in the online version of the paper.

Tong Li received her BSc degree from the School of Materials Science and Engineering, Shandong University of Science and Technology, in 2019. She is currently pursuing her MSc degree at the School of Materials Science and Engineering, Shandong University. Her current research focuses on the field of carbon materials and their applications in supercapacitors.

Jianjun Zhang received his BSc degree from the School of Materials Science and Engineering, Shandong University of Science and Technology, in 2015. He is currently pursuing his MSc degree at the School of Materials Science and Engineering, Shandong University. His current research focuses on the field of DFT calculations and light metal materials.

Jing Zhang is an associate researcher at the Advanced Materials Institute, Qilu University of Technology (Shandong Academy of Sciences). She received her PhD degree in materials science from Lanzhou University of Technology (2010). Currently, her research focuses on novel porous carbon materials for supercapacitors and gas adsorbents.

Zhao Qian is a professor at the School of Materials Science and Engineering, Shandong University. He received his PhD degree in materials physics from KTH Royal Institute of Technology, Sweden (2013). From 2015 to 2018, he worked as a postdoctoral fellow at Uppsala University, Sweden. Currently, his research focuses on DFT calculations and light metal materials.

Rutao Wang is a professor at the School of Materials Science and Engineering, Shandong University. He received his PhD degree in materials science from Lanzhou Institute of Chemical Physics, Chinese Academy of Sciences (2015). From 2013 to 2014, he joined Professor Li Zhang's group as a research fellow at the Department of Mechanical and Automation Engineering, The Chinese University of Hong Kong. Currently, his research focuses on advanced materials for supercapacitors and all-solid-state batteries.

高储锂性能的氮、磷共掺杂分级多孔炭纳米球用于高比能锂离子电容器

李桐[1†], 张建军[1†], 李崇兴[1], 赵涵[1], 张晶[2*], 钱钊[1*], 尹龙卫[1], 王儒涛[1,3,4*]

摘要 锂离子电容器通常由一个电池型负极和一个电容型多孔炭正极组成, 可输出比传统双电层电容器高两倍的能量密度, 但是在高倍率条件下其能量密度低、循环寿命短, 因而其广泛应用受到阻碍. 本文通过模板法合成了一种结构高度无序、氮/磷共掺杂的分级介孔炭纳米球. 这种分级多孔结构有利于锂离子的快速迁移, 且高度无序的结构和高杂原子含量为锂离子电荷存储提供了丰富的活性位点. 电化学测试表明, 该炭纳米球负极具有较高比容量(在0.1 A g^{-1}时, 为1108.6 mA h g^{-1}), 优异的倍率性能(在8 A g^{-1}时, 为276.5 mA h g^{-1}), 以及良好的循环稳定性(1000次循环后仍保持85%的容量). 以该分级多孔纳米球为负极, 自制活性炭为正极所组装的锂离子电容器具有较高的能量密度(103 W h kg^{-1})、功率密度(44,630 W kg^{-1})以及长循环寿命(>10,000圈). 该工作揭示了如何通过在纳米/原子尺度上调控炭材料微结构来提高电化学性能的方法, 为设计高性能的储能设备提供了新策略.

